Deformation Mechanisms, Microstructures, and Seismic Anisotropy of Wadsleyite in the Earth's Transition Zone

Estelle Ledoux, Morvarid Saki, Jeffrey Gay, Matthias Krug, Olivier Castelnau, Wen-yi Zhou, Jin S. Zhang, Julien Chantel, Nadege Hilairet, Maxim Bykov, et al.

Geochemistry, Geophysics, Geosystems®

AGU ADVANCING EARTH AND SPACE SCIENCES

RESEARCH ARTICLE
10.1029/2023GC011026

Key Points:

- Deformation mechanisms of wadsleyite at mantle transition zone (MTZ) pressure and temperature from multigrain diffraction in the diamond anvil cell
- <111>{101} is the most active slip system. Secondary systems depend on temperature and water content, and affect texture and anisotropy
- A new deformation map for wadsleyite at MTZ pressure and temperature

Supporting Information:

Supporting Information may be found in the online version of this article.

Correspondence to:

E. E. Ledoux and S. Merkel,
ledoux.estelle@outlook.fr;
sebastien.merkel@univ-lille.fr

Citation:

Ledoux, E. E., Saki, M., Gay, J. P., Krug, M., Castelnau, O., Zhou, W.-Y., et al. (2023). Deformation mechanisms, microstructures, and seismic anisotropy of wadsleyite in the Earth's transition zone. *Geochemistry, Geophysics, Geosystems*, *24*, e2023GC011026. https://doi.org/10.1029/2023GC011026

Received 27 APR 2023
Accepted 10 OCT 2023

Author Contributions:

Conceptualization: Nadège Hilairet, Carmen Sanchez-Valle, Christine Thomas, Sergio Speziale, Sébastien Merkel

Deformation Mechanisms, Microstructures, and Seismic Anisotropy of Wadsleyite in the Earth's Transition Zone

Estelle E. Ledoux[1,2], Morvarid Saki[3], Jeffrey P. Gay[1], Matthias Krug[4], Olivier Castelnau[5], Wen-Yi Zhou[6], Jin S. Zhang[6], Julien Chantel[1], Nadège Hilairet[1], Maxim Bykov[7,8], Elena Bykova[9,10], Georgios Aprilis[11], Volodymyr Svitlyk[12,13], Gaston Garbarino[12], Carmen Sanchez-Valle[4], Christine Thomas[3], Sergio Speziale[14], and Sébastien Merkel[1]

[1]Univ. Lille, CNRS, INRAE, Centrale Lille, UMR 8207 - UMET - Unité Matériaux et Transformations, Lille, France, [2]Now at Department of Geology and Geophysics, University of Utah, Salt Lake City, UT, USA, [3]Institute of Geophysics, University of Münster, Münster, Germany, [4]Institute of Mineralogy, University of Münster, Münster, Germany, [5]Laboratoire PIMM, UMR, CNRS 8006, ENSAM, CNAM, Paris, France, [6]Department of Geology and Geophysics, Texas A&M University, College Station, TX, USA, [7]Bayerisches Geoinstitut, University of Bayreuth, Bayreuth, Germany, [8]Now at Institute of Inorganic Chemistry, University of Cologne, Cologne, Germany, [9]Deutsches Elektronen-Synchrotron DESY, Hamburg, Germany, [10]Now at the Institut für Geowissenschaften, Goethe-Universität Frankfurt, Frankfurt am Main, Germany, [11]Laboratory of Crystallography, Materials Physics and Technology at Extreme Conditions, Universität Bayreuth, Bayreuth, Germany, [12]ESRF - The European Synchrotron, Grenoble, France, [13]Helmhotz-Zentrum Dresden-Rossendorf, Institute of Resource Ecology, Dresden, Germany, [14]GFZ German Research Centre for Geosciences, Potsdam, Germany

Abstract Wadsleyite is the dominant mineral of the upper portion of the Earth's mantle transition zone (MTZ). As such, understanding plastic deformation of wadsleyite is relevant for the interpretation of observations of seismic signals from this region in terms of mantle flow. Despite its relevance, however, the deformation mechanisms of wadsleyite and their effects on microstructures and anisotropy are still poorly understood. Here, we present the results of new deformation experiments on polycrystalline wadsleyite at temperatures of 1400–1770 K and pressures between 12.3 and 20.3 GPa in the laser-heated diamond anvil cell. We rely on multigrain X-ray crystallography to follow the evolution of individual grain orientations and extract lattice preferred orientations at the sample scale at different steps of the experiments. A comparison of experimental results of our work and the literature with polycrystal plasticity simulations, indicates that ⟨111⟩{101} is the most active slip system of dislocations in wadsleyite at all investigated conditions. Secondary slip systems such as [001](010), [100](001), and [100]{0kl}, however, play a critical role in the resulting microstructures and their activity depends on both temperature and water content, from which we extract an updated deformation map of wadsleyite at MTZ conditions. Lastly, we propose several seismic anisotropy models of the upper part of the MTZ, depending on temperature, geophysical context, and levels of hydration that will be useful for the interpretation of seismic signals from the MTZ in terms of mantle flow and water content.

Plain Language Summary The ductile rocks of the Earth mantle are deforming plastically under the effect of mantle convection. In return, the way minerals accommodate deformation impacts the properties of the whole rock and controls mantle flow. The deformation mechanisms of upper mantle minerals have been studied extensively. The behavior of minerals found deeper in the Earth, however, still remains debated and poorly understood. Wadsleyite, a high pressure polymorph of olivine, is the major phase of the upper part of the mantle transition zone (MTZ) (at 410–520 km depth) and then is suspected to control the deformation of that region of the mantle. Investigations of deformation mechanisms in wadsleyite have been scarce and, only made recently possible with in-situ measurements at relevant pressure and temperature. Using in-situ deformation experiments, literature results, and numerical simulations, we propose a new view of plastic deformation of wadsleyite in the Earth's MTZ. We show that it will be strongly affected by both temperature and water content. We then provide models that could be used for the seismic detection of its anisotropic behavior and mapping mantle flow using seismic measurements.

Formal analysis: Estelle E. Ledoux, Morvarid Saki, Jeffrey P. Gay, Matthias Krug, Olivier Castelnau, Wen-Yi Zhou, Jin S. Zhang
Funding acquisition: Carmen Sanchez-Valle, Christine Thomas, Sergio Speziale, Sébastien Merkel
Investigation: Estelle E. Ledoux, Jeffrey P. Gay, Matthias Krug, Julien Chantel, Nadège Hilairet, Maxim Bykov, Elena Bykova, Georgios Aprilis, Volodymyr Svitlyk, Gaston Garbarino, Sergio Speziale, Sébastien Merkel
Methodology: Estelle E. Ledoux, Sébastien Merkel
Project Administration: Sébastien Merkel
Supervision: Carmen Sanchez-Valle, Christine Thomas, Sébastien Merkel
Validation: Estelle E. Ledoux, Sébastien Merkel
Writing – original draft: Estelle E. Ledoux, Sébastien Merkel
Writing – review & editing: Estelle E. Ledoux, Morvarid Saki, Jeffrey P. Gay, Matthias Krug, Olivier Castelnau, Wen-Yi Zhou, Jin S. Zhang, Julien Chantel, Nadège Hilairet, Maxim Bykov, Elena Bykova, Georgios Aprilis, Volodymyr Svitlyk, Gaston Garbarino, Carmen Sanchez-Valle, Christine Thomas, Sergio Speziale, Sébastien Merkel

1. Introduction

Wadsleyite is one of the dominant minerals of the mantle transition zone (MTZ) (Ringwood, 1991). As such, the properties of wadsleyite are critical to understand the dynamics of this region of the Earth, located between 410 and 660 km depth, and its observation using seismic waves. The dynamics of the MTZ remains a topic of investigation but is believed to affect the global mantle convection, as illustrated, for instance, by the stagnation of some subducted slabs around 660 km (e.g., Fukao et al., 2001; Van Der Hilst et al., 1997). In addition, the MTZ is believed to play a critical role in the Earth's water cycle (e.g., Andrault & Bolfan-Casanova, 2022; Bercovici & Karato, 2003) and is hence critical in constraining the thermal and chemical evolution of the Earth. One of the most direct means to constrain mantle flow from observations is by measuring seismic anisotropy, which can be caused by (a) lattice-preferred orientation (LPO) of anisotropic mantle minerals due to mantle flow; or (b) strain-induced shape-preferred orientation of isotropic materials with highly contrasting seismic properties (e.g., Faccenda, 2014; Karato, 1998; Magali et al., 2021). In the Earth's MTZ, seismic anisotropy is measured, either at a global scale (e.g., Panning & Romanowicz, 2006) or locally in subduction zones (e.g., Foley & Long, 2011; Mohiuddin et al., 2015; Nowacki et al., 2015). The source of that anisotropy, however is still debated. Minerals such as pyroxenes represent only a small volume fraction of the MTZ (15 vol. % or less) and disappear before the 520 km depth discontinuity (Ringwood, 1991) and phases like garnet and ringwoodite are nearly isotropic at MTZ conditions (Mainprice et al., 2000). Wadsleyite is hence the best candidate as a possible source of deformation-induced anisotropy in the MTZ. Thus, information on the plastic behavior of wadsleyite is crucial to understand microstructures, anisotropy, and the interpretation of seismic signals from the MTZ to constrain mantle flow and history of the upper part of the MTZ.

Understanding the development of anisotropy and microstructures in polycrystalline materials requires an identification of the minerals' dominant slip systems as a function of parameters such as pressure, temperature, water content or strain rate. The most frequently observed active slip systems in deformed wadsleyite in electron microscopy are $\langle 111\rangle\{101\}$, [100](010), [100](001), [100]{011} and [100]{021} (Farla et al., 2015; Ohuchi et al., 2014; Sharp et al., 1994; Thurel & Cordier, 2003; Thurel et al., 2003, see Figure S1 in Supporting Information S1). Tommasi et al. (2004) then proposed visco-plastic self-consistent (VPSC) models of potential LPO in polycrystalline wadsleyite, testing different combinations of slip systems and relative critical resolved shear stress (CRSS) values based on these observations. At the time of the study, however, experimental LPO measurements on polycrystalline wadsleyite were not available and the models of Tommasi et al. (2004) could not be validated against experimental microstructural data.

Due to technical limitations, only few experimental studies have investigated LPO development in polycrystalline wadsleyite (Couvy, 2005; Demouchy et al., 2011; Farla et al., 2015; Kawazoe et al., 2013; Ohuchi et al., 2014). These deformation experiments have shown that different LPO patterns can be observed in wadsleyite (see Figure 1). Demouchy et al. (2011) showed that the texture measured in their experiments could be modeled in VPSC simulations with the activation of an additional [001](010) slip system. Ohuchi et al. (2014) then defined three types of microstructures and the corresponding controlling deformation mechanisms, depending on temperature and water content. Finally, Metsue et al. (2010) and Ritterbex et al. (2016) modeled dislocation glide in wadsleyite based on a multi-scale and multi-physics approach, focusing on the rate limiting $\frac{1}{2}\langle 111\rangle\{101\}$ and [100](010) dissociated screw dislocations. They provide key parameters to model dislocation glide in such systems, including estimates of their CRSS, which were then fed into multiscale calculations to model microstructural development in wadsleyite at the polycrystal scale (Castelnau et al., 2021). Despite these studies, however, a comprehensive model of wadsleyite LPO development at MTZ conditions, that could explain all experimental observations, is still lacking.

Here, we introduce new measurements of wadsleyite deformation microstructures using multigrain crystallography (MGC) in the laser-heated diamond anvil cell (LH-DAC). This method allows for sample deformation and LPO reconstruction, in-situ, at both the pressures and temperatures of the Earth's MTZ (although, as usual, at much higher strain-rates as those encountered in-situ). Polycrystalline wadsleyite was deformed in the 11.3–20.3 GPa and 1450–1730 K *P-T* range by axial compression induced by the LH-DAC. MGC was then used to extract individual grain orientations within the sample and study its microstructural evolution with deformation. We then implemented a state-of-the-art viscoplastic scale transition polycrystal model (denoted FOSO-VPSC) in order to interpret both our measurements and those of the literature in order to build a comprehensive scenario for wadsleyite deformation at MTZ conditions. We hence highlight the critical roles of both temperature and water content

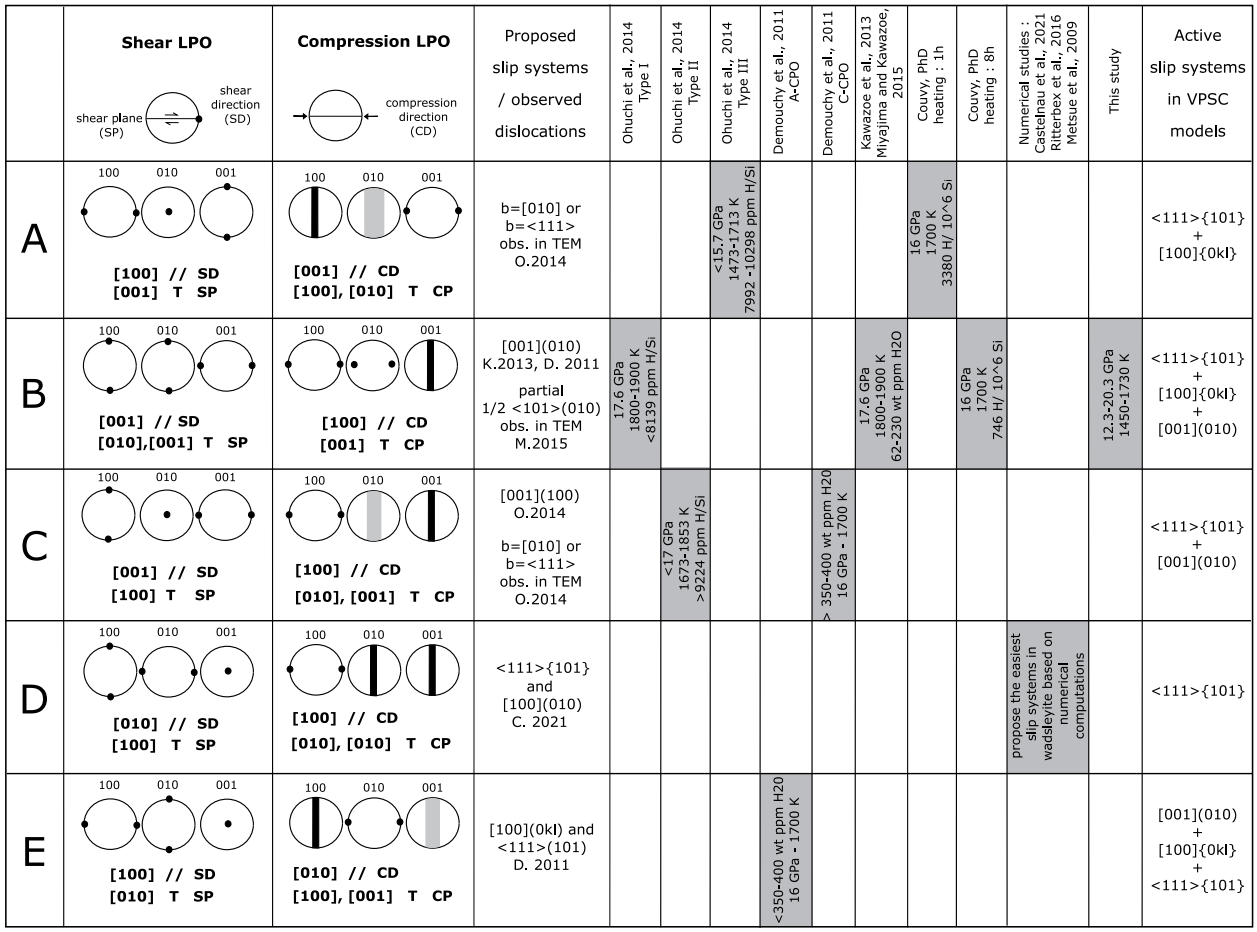

Figure 1. A- to E-type wadsleyite textures, corresponding observations, and dominant slip systems. Parameters for FOSO-VPSC simulations are listed in Table 2 and full corresponding textures and relative slip system activities plotted in Figure 4 and Figure S4 in Supporting Information S1, respectively.

on dominant slip systems in wadsleyite and the induced microstructures. Finally, we propose a model for seismic anisotropy in the upper part of the Earth's MTZ, both under dry and hydrous conditions, that can be used for the interpretation of potential anisotropy observations in terms of mantle flow.

2. Materials and Methods

2.1. Sample Preparation and High *P-T* Experiments

San Carlos olivine crystals were ground in a planetary mill and then sintered in a piston-cylinder between 500 and 600 MPa at 1500 K for a duration of 40 min. The sintering product consists in a pure olivine polycrystal and electron microscopy characterization shows it has a heterogeneous grain size distribution, ranging between less than a micron and up to 50 µm, with no preferred orientation (Figure 2a). The water content in the sintered material is less than 3 ppm, as measured by infrared spectroscopy in olivine grains within the sintered polycrystal. After the sintering, the product was cut with a precision diamond wire saw into fine slices. These slices were then mechanically polished to a thickness of 10–15 µm. Finally, disks of 20 µm diameter were cut out of these slices using pulsed lasers, and coated with 150–200 nm platinum layers on both sides to ensure a proper absorption of the heating infra-red lasers of the LH-DAC by the sample.

The 20 µm diameter olivine samples were then loaded under controlled argon atmosphere into a DAC equipped with diamonds with 300 µm flat culets and a rhenium gasket with holes of 100–145 µm in diameter to serve as the sample chamber (Figure 2b). We employed either MgO or KCl as pressure medium, for both their lack of chemical reaction with olivine or wadsleyite and their melting temperature above our target temperatures in the

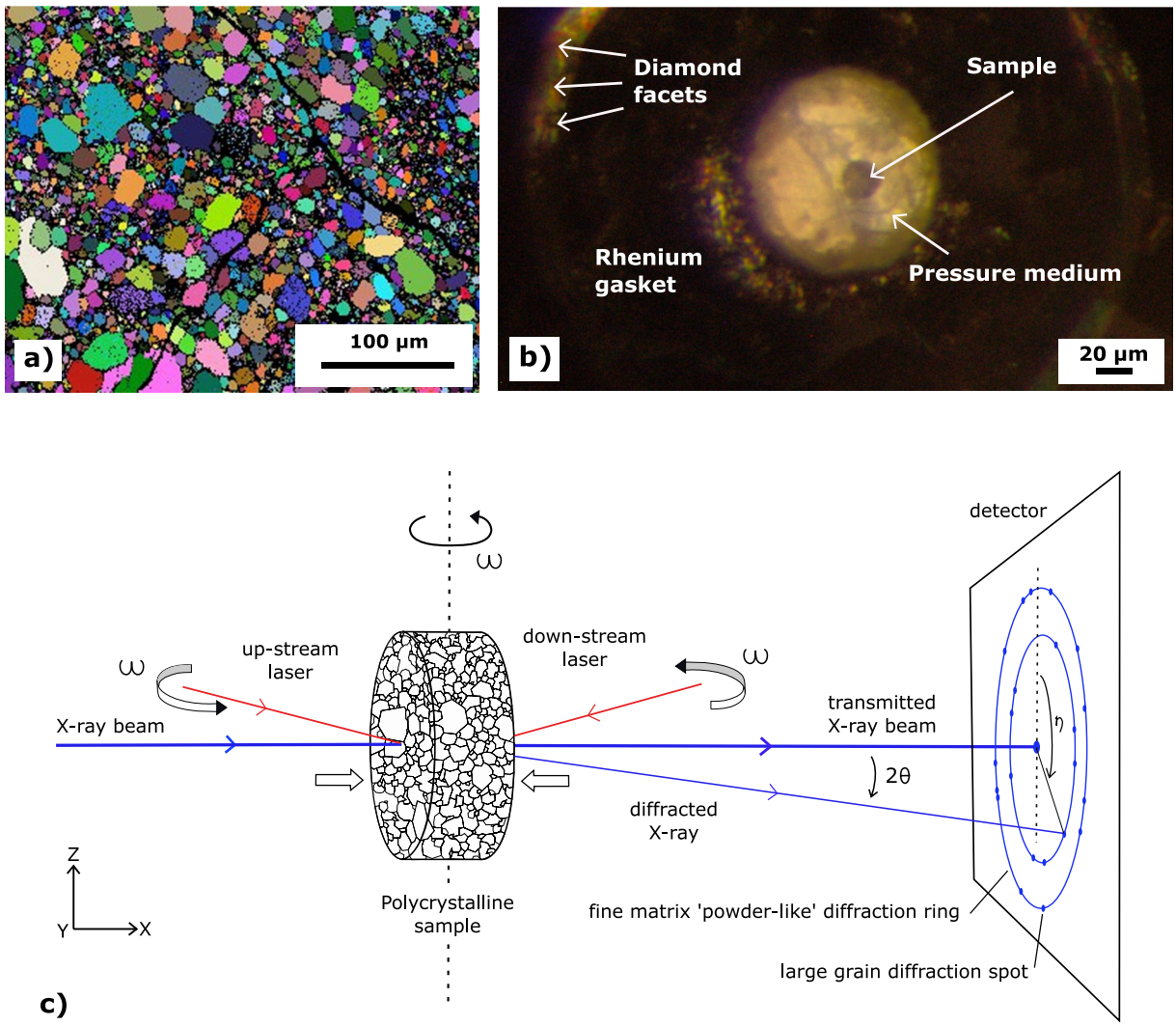

Figure 2. (a) Starting material characterization and (b and c) experimental setup for deformation and in-situ multigrain crystallography experiments. (a) Electron backscattered diffraction (EBSD) orientation map of the starting material after sintering. Each color corresponds to a different lattice orientation. (b) Experimental loading in the DAC. The sample is a 20 µm diameter disk cut from the starting material in (a). (c) Multigrain crystallography experimental set-up. The wadsleyite polycrystalline sample is compressed at mantle transition zone pressures and temperatures in the laser-heated diamond anvil cell. The compression direction is along X (wide empty arrows). The synchrotron X-rays beam (thick blue line) passes through the DAC and is transmitted or diffracted by the crystallites in the sample. The diffracted rays (thin blue lines) form the diffraction pattern on the detector. The DAC is rotated in ω and data are collected at different ω values. The laser heating system (red lines) is rotating with the DAC during ω rotations.

10–20 GPa pressure range (Kimura et al., 2017; Shen & Lazor, 1995; D. Zhou et al., 2020). Membranes were used to control sample pressure remotely.

The state of the sample was monitored by in-situ multigrain X-ray diffraction at the ID27 beamline of the ESRF and the P02.2 beamline at PETRA III. In all experiments, the polycrystalline olivine sample was loaded at ambient temperature up to 2–7 GPa, after which it was laser-heated at temperatures of 1400–1800 K. The sample was then maintained at high temperature while pressure was slowly increased. Single-exposure X-ray diffraction was used to estimate pressure and the presence of olivine or wadsleyite. At several points upon compression, pressure increase was stopped to collect multigrain X-ray diffraction data by rotating the DAC over $\Delta\omega \approx 60°$ (depending on diamond thickness and cell opening) and acquiring X-ray diffraction images at every 0.5° increment of rotation $\delta\omega$ (Figure 2c). At both ERSF-ID27 and PETRA-III-P02.2, laser heating was maintained during multigrain X-ray diffraction data collection using a setup such as in Kupenko et al. (2012) at PETRA III and a similar layout at ESRF.

Table 1
Pressure and Temperature Conditions for Compression Experiments on Wadsleyite

Run	Point	P (GPa)	T (K)	N	GR (μm)
LTC_05_01	s27	18.7(7)	1730	114	0.6(3)
	s28	8.9	300	560	0.4(2)
LTC_03_02	s08	18.8(3)	1700	188	0.5(2)
	s09	18.8(7)	1620	208	0.3(2)
	s10	20.3(7)	1700	232	0.5(2)
	s12	13.1	300	251	0.5(2)
P2_01	s08	12.3(7)	1450	144	0.7(3)
	s09	14.0(7)	1520	136	0.8(3)
	s15	14.8(7)	1510	99	0.8(3)

Note. Numbers in parenthesis are uncertainties on the last digit of the computed pressure, estimated using a 100 K uncertainty on the temperatures. N is the number of grain indexed by multigrain crystallography, and GR is the mean grain radius extracted from MGC, with uncertainties on the last digit in parenthesis.

At the P02.2 beamline at PETRA III (Liermann et al., 2015), X-rays were set to a wavelength of 0.2903 Å and focused to 7.6 (horizontal, H) by 4.4 (vertical, V) μm^2. The sample to detector distance was of 398.7 mm, based on the CeO_2 calibration. Diffraction images were collected using a Perkin-Elmer XRD 1621 amorphous silicon flat-panel detector with 2,048 × 2,048 pixels of 200 × 200 μm^2 size for 5 s. At the ID27 beamline at ESRF (Mezouar et al., 2005), we used X-rays with a wavelength of 0.3738 Å, focused to 3.2 (H) by 3.0 (V) μm^2. The sample to detector distance was of 245.54 mm, based on the CeO_2 calibration. Diffraction images were collected using a MAR165 CCD planar detector with 2,048 × 2,048 pixels of 80 × 80 μm^2 size for 6 s.

2.2. Experimental Data Analysis

Sample temperatures were measured using spectral radiometry as provided by the beamlines during the experiments. The pressure and sample composition was monitored from the 2D-diffraction patterns using Dioptas (Prescher & Prakapenka, 2015). Post-experiment, ω-rotation multigrain diffraction images were stacked to generate an average diffraction image, which was then further processed using the Rietveld refinement package MAUD (Lutterotti et al., 2014; Wenk et al., 2014) from which we extract the unit cell parameters of the pressure medium, olivine, and wadsleyite. Pressure was then calculated using thermal equations of state from the literature (Angel et al. (2018) for olivine and Katsura et al. (2009) for wadsleyite) and the EosFit Calculator software (Angel et al., 2014).

Stress and strain rate in diamond anvil cell experiments can be difficult to quantify. Based on comparison between the strength of our experimental textures and VPSC simulations, we can estimate the total applied axial strain to be on the order of 50%. As each compression lasted for 3–15 hr, the strain rates should hence be on the order of 1–5 × 10^{-5} s^{-1}. Those experiments rely on continuous compression in the DAC, and thus the resulting strain rates are similar to those in multi-anvil experiments. For stress determination in our samples, we faced two issues, (a) our samples consist of individual "single" crystals and so present a strongly spotty pattern that the classical powder diffraction analysis methods are difficult to handle, and (b) in axial geometry stress determination is not straightforward as it only appears as small shifts of the diffraction peak positions. To overcome the first issue, we tried to refine stress in the pressure media, which present a more powder-like diffraction signal and can be processed using a Rietveld refinement. The fit resolution, however, was insufficient to report reliable stresses in either MgO or KCl pressure media.

For run LTC_05_01, performed at ESRF, wadsleyite was formed from olivine while increasing pressure between 14.9 and 18.7 GPa and temperature between 1400 and 1730 K. For ESRF run LTC_03_02, wadsleyite was formed from olivine while increasing pressure between 17.0 and 18.0 GPa at 1700 K. Finally, for run P2_01, performed at PETRA III, wadsleyite was formed from olivine after over-pressurizing to 20.3 GPa and releasing pressure to 12.3 GPa at temperatures between 1450 and 1550 K. Pressure and temperature conditions for all MGC measurements on wadsleyite are then summarized in Table 1.

The sample microstructural evolution with increasing pressure and deformation is analyzed using MGC. This method consists in acquiring 2D-diffraction images while rotating the sample in ω. The data are then processed to (a) separate the individual diffraction spots of the grains of the sample large enough to produce a single-crystal-like signal, from the rest of the signals, which includes powder-like diffraction signal of the smaller sample grains, signal from the pressure medium, diamond Compton scattering, etc., (b) identify these extracted diffraction spots, and (c) determine the grain orientation matrices. The detailed procedure has been described in Rosa et al. (2015) and used in several publications (Chandler, Bernier, et al., 2021; Chandler, Devoe, et al., 2021; Gay et al., 2023; Krug et al., 2022; Langrand et al., 2017; Rosa et al., 2016).

Data analysis relies on open-source software from the FABLE-3DXRD package, available online at https://github.com/FABLE-3DXRD, additional tools from the TIMEleSS project, available online at https://github.com/FABLE-3DXRD/TIMEleSS, and thoroughly described in a dedicated manual at http://multigrain.texture.rocks/. The exact workflow to process multigrain images for olivine and wadsleyite is presented in a companion paper, focusing on transformation microstructures between olivine and wadsleyite (Ledoux, Krug, et al., 2023). The final output

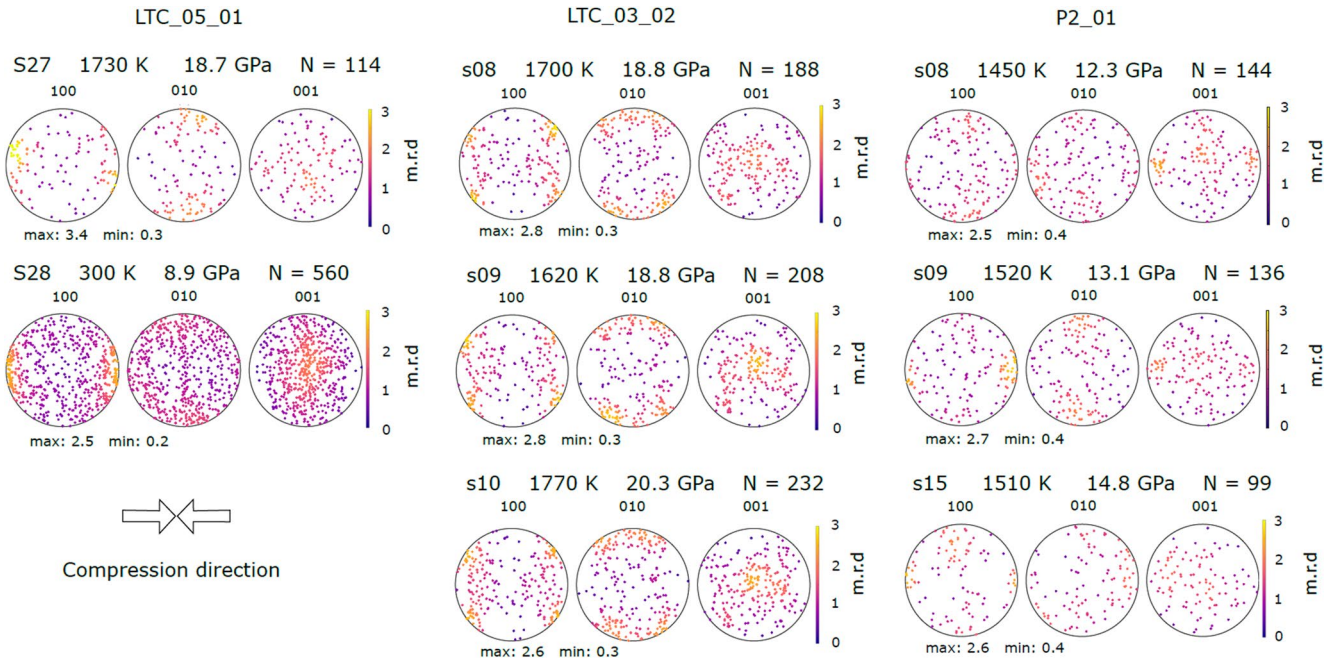

Figure 3. Pole figures (PF) representing grain orientations measured in-situ by multigrain crystallography during deformation experiments on wadsleyite in the laser-heated diamond anvil cell. Each dot in a PF corresponds to the orientation of one wadsleyite grain of the sample. The color of the marker corresponds to the probability of the orientation, recalculated from an orientation density function (ODF) fitted to the sample grain orientations. For each measurement, the name of the measurement (s), the temperature during the measurement, the pressure during the measurement, and the number of indexed grains (*N*) are indicated above the PF. Minimum and maximum intensity for each group of PF are indicated. The corresponding inverse PF of the compression direction are shown in Figure S2 of Supporting Information S1. For an easier visualization of texture and comparison with previous EBSD measurement, we also provide smoothed PF recalculated from the ODF fitted to our data in Figure S3 of Supporting Information S1.

of the multigrain images treatment consists in a list of grains, defined by their unit cell parameters and crystallographic orientation and the list of the associated diffraction spots. Individual grain orientations are then plotted as pole figures (PF, Figure 3) or inverse pole figures (IPF) of the compression direction (Figure S2 in Supporting Information S1). In addition, using the intensity of the diffraction spots and the geometry of the experiment, the size of each indexed grain have been estimated, and the mean grain radii in our samples are given in Table 1.

2.3. FOSO-VPSC Modeling

We modeled the effect of plastic deformation by dislocation glide on wadsleyite textures using a recent version of the nonlinear VPSC model, more accurate than the original version of Lebensohn and Tomé (1993) usually denoted as VPSC in the literature. This model has been developed by Ponte Castañeda (2015) and Song and Ponte Castañeda (2018), and is denoted as Fully Optimize Second Order viscoplastic self consistent scheme (FOSO-VPSC). In short, the model aims at estimating the behavior of the polycrystalline aggregate from the behavior of individual crystals and the microstructure (LPO, grain shape). When using a mean-field model such as VPSC, one has to linearize appropriately the crystal constitutive relation, and this is a difficult task, as explained for instance in Castaneda and Suquet (1997). The original VPSC model of Lebensohn and Tomé (1993) violates an exact bound and is thus not well adapted for strongly anisotropic materials as considered here (e.g., Lebensohn et al., 2011). With respect to this difficulty, the FOSO-VPSC model is more accurate, in particular it complies with rigorous upper bounds and lacks duality gap, that is, stress and strain-rate formulations yield identical results. It has been shown to provide results that lie very close to full-field computational scale transition (at a significantly lower numerical effort), even for highly anisotropic materials. A first application to Earth mineral (wadsleyite as here) has been proposed in Castelnau et al. (2021).

Here, we used a starting virtual sample composed of 5,000 randomly oriented grains with equiaxed shape, deformed with increments of deformation of $\varepsilon = 0.05$ with a strain rate of 1×10^{-5} s^{-1}. The shape of the grain was free to evolve during the deformation. The stress sensitivity was fixed to $n = 3.5$. Simulations were performed

10.1029/2023GC011026

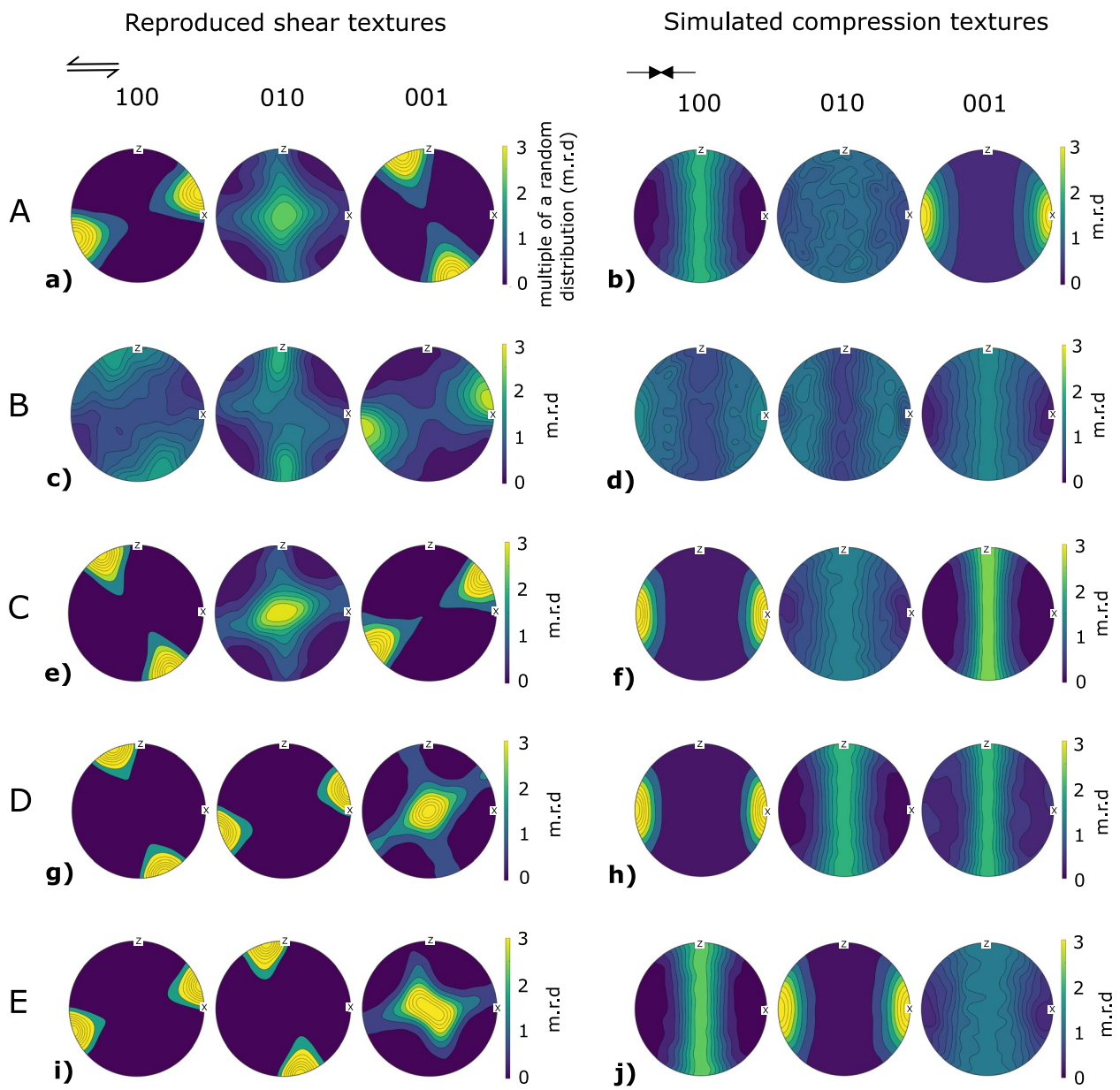

Figure 4. FOSO-VPSC texture simulations. Simulated textures in shear (a, c, e, g, i) and compression (b, d, f, h, j) corresponding to Models A, B, C, D, and E in Table 2. Textures in shear are for $\gamma = 1$ and textures in compression are for $\epsilon = 0.5$. The pole figures are plotted onto the lower hemisphere.

both in compression and in shear. Simulations in compression used a total strain of $\epsilon = 0.5$ while simulations in shear used a total strain of $\epsilon = 1$. The textures resulting from these simulations are reported in Figure 4.

Based on previous studies, we considered the ⟨111⟩{101}, [100](010), [100](001), [100]{011}, [100]{021} and [001](010) slip systems. Starting from the models of Tommasi et al. (2004) and Demouchy et al. (2011), we then optimized a combination of relative CRSS values using trial and error in order to reproduce experimental texture observations from this work and the literature (Figure 1) and generated five independent models that will be discussed later in the manuscript. The combination of slip systems and associated relative CRSS values for those five models are given in Table 2.

Table 2
Relative Critical Resolved Shear Stress (CRSS) Values for the A, B, C, D, and E Visco-Plastic Self-Consistent Models for Wadsleyite

Texture	Slip system	⟨111⟩ {101}	[100] (010)	[100] (001)	[100] {011}	[100] {021}	[001] (010)
Type A	CRSS	50	10	10	10	10	1,000
	Activity (%)	54	6	10	16	14	0
Type B	CRSS	50	100	100	100	100	10
	Activity (%)	52	2	6	8	5	27
Type C	CRSS	50	1,000	1,000	1,000	1,000	10
	Activity (%)	80	0	0	0	0	20
Type D	CRSS	10	30	1,000	1,000	1,000	1,000
	Activity (%)	100	0	0	0	0	0
Type E	CRSS	1,000	10	10	10	10	50
	Activity (%)	15	8	10	18	17	32

Note. The reported relative activities of the slip systems are obtained at the end of the simulation in shear up to $\gamma = 1$. In this study, we use a stress sensitivity of $n = 3.5$ for the viscoplastic behavior.

2.4. Grain Orientations Analysis and Seismic Anisotropy Modeling

Indexed grain orientations are shown as pole figures (Figure 3) and inverse pole figures (Figure S2 in Supporting Information S1), using the open-source MTEX toolbox for MATLAB (Bachmann et al., 2010). In these figures, each marker represents the orientation of a single indexed grain. Markers are color-coded according to intensities deduced from an orientation density function (ODF) fitted to the individual grain orientations in MTEX. To help visualize the sample texture and comparison with other measurements such as EBSD, we also provide smoothed pole figures recalculated from the ODF computed from our experimental orientations (Figure S3 in Supporting Information S1). MTEX is also used to plot the results of FOSO-VPSC simulations, using ODF calculated from the orientations of the 5,000 orientations at the end of the simulation ($\gamma = 1$ for shear, $\epsilon = 0.5$ for compression, Figure 4).

Seismic anisotropy calculations are performed within MTEX. We computed the aggregate properties of textured wadsleyite from the grain orientations in the FOSO-VPSC model and single-crystal elastic moduli using a Reuss-Voigt-Hill averaging scheme. Two sets of single crystal elastic moduli are used in this study: a set of computed elastic moduli for dry wadsleyite (Núñez-Valdez et al., 2013) and a set of elastic moduli measured in hydrous wadsleyite (W.-Y. Zhou et al., 2022). Also note that comparison will be provided with the set of elastic moduli computed for hydrous wadsleyite in the study of W. Wang et al. (2019). For dry wadsleyite, the elastic moduli were calculated using first-principle computation (Núñez-Valdez et al., 2013) and are available at http://mineralscloud.com/resources/thermoelasticityofminerals/index.shtml. For hydrous wadsleyite, the elastic moduli were measured for hydrous Fe-bearing wadsleyite using Brillouin spectroscopy up to 16.6 GPa and 700 K (W.-Y. Zhou et al., 2022) and extrapolated at 15 GPa and 1500 and 1800 K. All the single crystal elastic moduli we used are provided in Table S1 of Supporting Information S1. The elastic moduli for the polycrystal we computed using the LPO obtained by our FOSO-VPSC simulations (Figure 4) and the single crystal elastic moduli from the literature (Table S1 in Supporting Information S1), are reported in Table S2 of Supporting Information S1, for both hydrous and dry wadsleyite. Seismic wave velocities V_P and V_S, shear wave splitting ΔV_S and fast shear wave polarities were then calculated from the aggregate properties of textured wadsleyite using a density determined by W.-Y. Zhou et al. (2022).

3. Results

3.1. Wadsleyite Deformation Microstructures in the LH-DAC

Our multigrain measurements generally index 100 to 250 single grains of wadsleyite (e.g., Table 1), with an exception for run LTC_05_01 after temperature quench for which the number of indexed grains increases up to 560. In run LTC_03_02, the number of indexed grains increases slightly with increasing pressure, while it decreases during compression in run P2_01.

For run LTC_05_01, transformed at 1730 K and 18.7 GPa, wadsleyite grains measured after transformation from olivine show a texture with the [100] crystallographic direction preferentially aligned near the compression direction and their [010] crystallographic axis preferentially aligned in a large girdle around the compression plane, with maximas at low angle of the Z axis of the pole figure (Figure 3). The [001] crystallographic axis generally aligns normal to compression direction. Upon temperature quench, grain size in the sample slightly decrease from 0.6 μm in measurement s27 to 0.4 μm in measurement s28. In parallel, we observe an increase of the number of indexed grains, together with a strengthening of texture with [100] axis preferentially aligned with the compression direction.

In run LTC_03_02, transformed at 1700 K and 18.8 GPa, orientations of the wadsleyite grains after the transformation show a texture with the [100] crystallographic axis at 30–40° of the compression direction, the [010] axis forming a wide girdle in the compression plane with maxima at ≈ 30° of the Z axis of the pole figure and the [001] axis aligning normal to the compression direction (Figure 3). The post-transformation texture in that sample does not evolve significantly upon further compression and deformation. Mean grain

radius in the sample does not evolve significantly during the deformation, and remains on the order of 0.5 μm, except for LTC_03_02_s09 in which the grain size is slightly smaller (0.3 μm), maybe due to a drop in temperature.

In run P2_01, transformed at lower temperature (1500–1510 K) and pressure (12.3 GPa), the texture after transformation is weak, with a maximum for orientations with the [001] crystallographic axis parallel to the compression direction. Texture strengthens upon further compression and evolves toward a maximum with [100] parallel to the compression direction, as in the other runs. The [010] crystallographic axes weakly and inconsistently align normal to the compression direction, while [001] axes do not show any consistent preferred orientations (Figure 3). In this sample, the mean grain radius slightly increases with further deformation, from 0.7 μm in measurement s08 to 0.8 μm in measurements s09 and s15.

Overall, our measurements can be sorted in two types of textures. Samples LTC_05_01 and P2_01 have a similar texture, characterized by an alignment of the [100] crystallographic axes along the compression direction and the [010] axis aligned in the compression plane. In sample LTC_03_02, the main features of the LPO are the [100] axis preferentially oriented at 30–40° of the compression direction and the [010] axis oriented at ≈20–30° of the compression plane.

Average grain sizes in our samples range from 0.3 to 0.8 μm in equivalent radius and do not seem to drastically change during deformation. These ranges of grain sizes are in the lower end of other deformation experiments on wadsleyite (0.2–50 μm, Demouchy et al. (2011), Kawazoe et al. (2013), Ohuchi et al. (2014), and Farla et al. (2015)).

3.2. Interpretation of Our Experimental Texture

Our experimental results show that, in the 12.3–20.3 GPa and 1450–1730 K *P*–*T* range, axial compression on polycrystalline wadsleyite can produce two different LPO, one with the [100] axis aligned in the compression direction, the [010] axis aligned in the compression plane and the [001] axis normal to the compression direction, and an other one with the [100] axis oriented at 30–40° of the compression direction, the [010] axis oriented at 20–30° of the compression plane and the [001] axis normal to the compression direction. Olivine to wadsleyite transformation is mostly dominated by a diffusive mechanism for which inheritance of LPO is unlikely to be significant (Smyth et al., 2012). This statement is confirmed within our experiments, in which no specific crystallographic relationship have been observed between pre-transformation olivine and post-transformation wadsleyite (see companion paper by Ledoux, Krug, et al. (2023)). In addition, LPO does evolve with sample compression (e.g., run P2_01). As such, they can safely be assigned to plastic deformation in wadsleyite.

These textures cannot be reproduced by the VPSC models suggested in previous studies (Demouchy et al., 2011; Tommasi et al., 2004). We hence designed new sets of relative CRSS values for VPSC simulations to match experimental observations.

The experimental texture observed in sample LTC_03_02 is well reproduced when slip on [001](010) is 5 times easier than slip on ⟨111⟩{101}, and 10 times easier than slip on [100](010), [100](001), [100]{011}, [100]{021} (for convenience, slip systems with [100] slip direction will be designated altogether by [100]{0kl}). Results of FOSO-VPSC simulations in compression are shown in Figure 4 and the optimized CRSS value combination is that of Model B in Table 2. FOSO-VPSC simulations indicate that ⟨111⟩{101} is the most active slip system for this LPO, followed by [001](010), and that the [100]{0kl} systems have a weak activity (Table 2, Figure S4 in Supporting Information S1).

The experimental texture observed in samples LTC_05_01 and P2_01 is reproduced when slip on [001](010) is 5 times easier than slip on ⟨111⟩{101}, and 100 times easier than slip on [100]{0kl}. The simulated texture is presented in Figure 4, and the corresponding CRSS are given in Table 2, as model C. The simulation indicates that for this LPO the most active slip system is ⟨111⟩{101}, followed by [001](010), and that the [100]{0kl} systems are not active at all (Table 2, Figure S4 in Supporting Information S1).

4. Plasticity of Polycrystalline Wadsleyite

4.1. Literature Results: Analysis and Re-Interpretation

Multiple texture types have been reported for wadsleyite in the literature, and most have been observed using experiments in a shear geometry. On the basis of VPSC simulations and electron microscopy observations, Tommasi et al. (2004) defined multiple potential texture types for wadsleyite. Later, the study of Ohuchi et al. (2014) defined Type-I, Type-II and Type-III to label the three textures types observed in their study and that of Kawazoe et al. (2013). In addition, Demouchy et al. (2011) reported a new texture type ("A-CPO") and used yet another notation. Finally, there are reports of weak textures in Farla et al. (2015), which are strongly affected by compression prior to deformation in shear.

We hence attempt to clarify this situation by introducing wadsleyite models A, B, C, D, E to harmonize the textures and plasticity models labeling for wadsleyite. All models are built against FOSO-VPSC simulations (Table 2) and hence identify the controlling deformation mechanisms. These five plastic models for wadsleyite allow reproducing texture types and numerical models found in the literature. Modeled textures and observations for each plastic model are listed in Figure 1, the resulting pole figures and relative slip system activities plotted in Figure 4 and Figure S4 of Supporting Information S1, and are described below.

Plastic model Type-A is produced using relative CRSS values of 50:10:1000 for ⟨111⟩{101}, [100]{0kl} and [001](010), respectively, similar to the values proposed in model 2 of Tommasi et al. (2004). Based on FOSO-VPSC simulation results, this texture is dominated by slip on the ⟨111⟩{101} and [100]{0kl} systems (Figure S4a in Supporting Information S1). [001](010) is not activated in this model. This produces a texture with [100] axes preferentially aligned toward the shear direction, [001] axes normal to the shear plane and [010] axis normal to the shear direction in the shear plane. It was observed in the study of Couvy (2005) and Ohuchi et al. (2014).

Plastic model Type-B is produced by activating all the considered slip systems with relative CRSS values of 50:100:10 for ⟨111⟩{101}, [100]{0kl} and [001](010), respectively. It reproduces our experimental compression textures in sample LTC_03_02. The plastic activity is dominated by those of ⟨111⟩{101} and [001](010), with limited activity of [100]{0kl} (Figure S4b in Supporting Information S1). In shear, [001] axes preferentially aligned toward the shear direction and [100] and [010] axes normal to the shear direction. Textures produced by plastic model Type-B are observed in this work and those of Kawazoe et al. (2013) and Ohuchi et al. (2014). These simulation results are in good agreement with the previous study of Kawazoe et al. (2013) in which [001](010) has been proposed as the dominant slip system to produce a Type-B texture. Miyajima and Kawazoe (2015) did not observe [001](010) dislocations when they analyzed one of the recovered Type-B textured sample by electron microscopy, but have demonstrated instead that slip on [001](010) happened in that sample by glide of dissociated partial $\frac{1}{2}\langle 101\rangle$ dislocations on (010).

Plastic model Type-C is generated with relative CRSS values of 50:1000:10 for ⟨111⟩{101}, [100]{0kl} and [001](010), respectively. It reproduces our experimental textures in samples LTC_05_01 and P2_01. This leads to slip activity dominated by ⟨111⟩{101}, secondary activity on [001](010), and no activity on [100]{0kl} (Figure S4c in Supporting Information S1). Type-C produces textures with [001] axes preferentially aligned toward the shear direction, [100] axes normal to the shear plane and [010] axes normal to the shear direction in the shear plane. It was observed in Demouchy et al. (2011) and Ohuchi et al. (2014).

Model Type-D is based on the activity of the ⟨111⟩{101} and [100](010) systems only, with relative CRSS values of 10:30, respectively, as proposed in Ritterbex et al. (2016) and, with slightly different CRSS values, in model 4 of Tommasi et al. (2004). The resulting texture is characterized by preferred orientation of the [010] axis toward the shear direction, the [100] axis normal to shear plane and the [001] axis normal to shear direction in shear plane (Figure 4g). It was not observed as such in published experimental results.

Finally, Type-E is built using CRSS of 1000:10:50 for systems ⟨111⟩{101}, [100]{0kl} and [001](010), respectively, similar to Demouchy et al. (2011). In this model all slip systems are active, but contrary to model B, [001](010) is the most active slip system (Figure S4e in Supporting Information S1). It was observed in Demouchy et al. (2011).

The relevance of each model, depending on deformation conditions, will now be discussed below.

4.2. A New Deformation Map for Wadlseyite at Transition Zone Conditions

As first hypothesized by Ohuchi et al. (2014), the diversity in observed wadsleyite textures can be understood by accounting for the effects of water content and temperature. Within the relatively small wadsleyite stability pressure range (i.e., 13–18 GPa), pressure does not seem to affect the observed microstructures types significantly. The effects of strain rate and stress on the deformation textures can not be assessed at this point, neither based on our DAC experiments nor with literature results. Ohuchi et al. (2014), however, did not observe any effect of strain rate on wadsleyite LPO in their experiments performed in the multi-anvil press.

Figure 5 presents a map of the experimental textures observed in wadsleyite plotted against temperature and water content. The deformation map shows a clear trend of texture changes depending on temperature and water content. Type-A texture is observed at low temperature (<1700 K) and low water content (below 700 wt ppm H_2O) whereas Type-B texture is observed at low water content (<600 wt ppm H_2O) and high temperature (>1700 K). At high temperature (>1700 K) and high water content (>600 wt ppm H_2O) texture Type-C is observed. Type-E texture seems to be an intermediate between type A and type B textures, both based on texture geometry (Figure 1) and slip systems activity (see below).

Based on that deformation map, we can hypothetize that the different observed LPO in our samples may be due to the presence of water in the sample chamber, possibly introduced during loading of the sample in the DAC and water content in the pressure medium. Unfortunately, we do not have measurements to verify that hypothesis.

The deformation map also shows the list of active slip systems for each texture type, as extracted through FOSO-VPSC models:

- At low temperature and low water content (texture Type-A), the dominant slip systems are ⟨111⟩{101} followed by [100]{0kl}.
- With increasing temperature (texture Type-B), the [001](010) slip system is activated in addition to ⟨111⟩{101} and [100]{0kl}.
- At high water content, the family of [100]{0kl} systems become inactive and deformation is controlled by dominant ⟨111⟩{101} and secondary [001](010).
- Texture Type-E is a transition between Type-A and Type-B with a lower activity of ⟨111⟩{101} and activity on both the [001](010) and [100]{0kl} systems.

Plastic model Type-D, arising from multiscale numerical models (e.g., Ritterbex et al., 2016), is not observed in experiments. The texture type is generated from a largely dominant activity of ⟨111⟩{101} with a weak contribution of the other systems (Figure S4d in Supporting Information S1). The ⟨111⟩{101} slip system is indeed active and dominant in most other plastic models and texture types, but is always activated together with secondary slip systems which, in fact, strongly affect the resulting texture. Hence, directly deducing active slip systems from LPO measurements in wadsleyite is not as straightforward as for olivine (Karato et al., 2008), for instance. This is due to the high number of symmetry equivalents in the ⟨111⟩{101} family of slip systems that induces complex and competing rotations at the crystal scale, which can be affected by small contributions of secondary slip systems.

Nevertheless, Figure 5 finally proposes a somewhat complete overview of plasticity and deformation microstructures in wadsleyite, with an understanding of the relative effects of both temperature and water content. Changes in dominant slip systems with temperature or water content can clearly explain the observed diversity in wadsleyite deformation textures. In most cases, ⟨111⟩{101} is the most active slip system, but the final microstructures are affected by secondary slip systems that do change with both water content and temperature.

5. Seismic Anisotropy and Implications for the Earth's Mantle Transition Zone

Wadsleyite is the major component of the upper portion of the MTZ and does show single-crystal elastic anisotropy (Núñez-Valdez et al., 2011, 2013; J. S. Zhang et al., 2018; W.-Y. Zhou et al., 2021). Other volumetrically important phases include garnet, pyroxenes, and ringwoodite (Ringwood, 1991). The contribution of those phases to anisotropy in the MTZ, however, is likely to be well below that of wadsleyite (Mainprice et al., 2000). As such, the effect of other phases would mainly be to dilute the anisotropic signal of deformed wadsleyite.

10.1029/2023GC011026

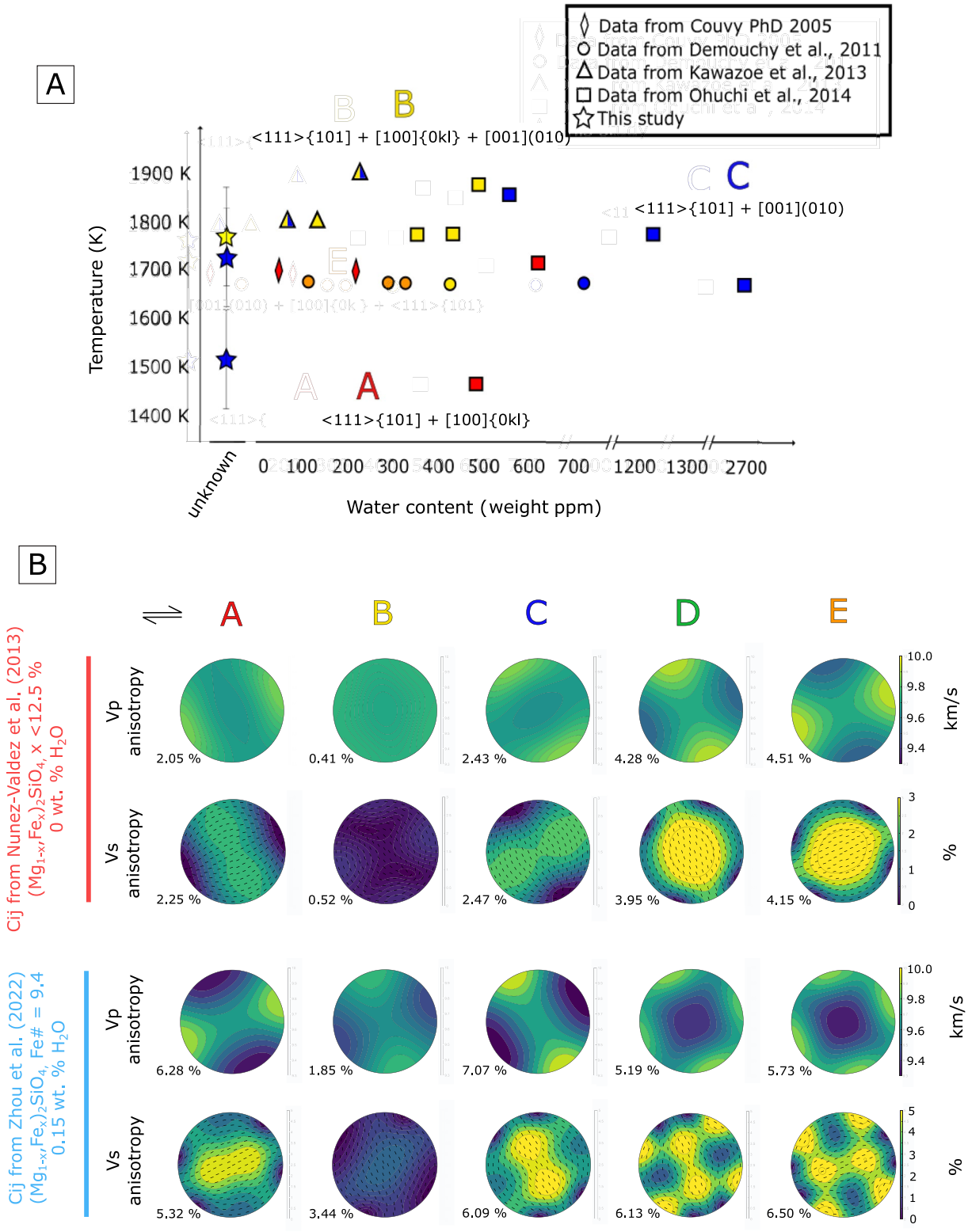

Figure 5.

5.1. Effect of Water on the Single Crystal Elasticity of Wadsleyite

Single crystal elastic moduli are required to compute seismic anisotropy in the deformed polycrystal. Numerous sets of elastic moduli for wadsleyite can be found in the literature (e.g., Buchen et al., 2018; Kiefer et al., 2001; Mao et al., 2008, 2011; Núñez-Valdez et al., 2011, 2013; Sinogeikin et al., 1998; J. Wang et al., 2014; W. Wang et al., 2019; W.-Y. Zhou et al., 2021, 2022). Only few, however, have been determined at both high P and high T (Núñez-Valdez et al., 2013; W. Wang et al., 2019; W.-Y. Zhou et al., 2022). Núñez-Valdez et al. (2013) and W. Wang et al. (2019) used first principle computations for dry and hydrous wadsleyite, respectively. W.-Y. Zhou et al. (2022) then reported the first experimentally determined elastic moduli measured at both high P and high T, with a study on hydrous wadsleyite (0.15 wt.% H_2O) using Brillouin spectroscopy up to 16.6 GPa and 700 K, then extrapolated to higher P-T conditions.

The choice of elastic moduli strongly impacts seismic signal computations. Figure 5b, for instance, shows seismic anisotropy of polycrystalline wadsleyite after 100% shear deformation computed for the A–E plasticity models using both the single crystal elastic moduli from Núñez-Valdez et al. (2013) ("dry wadsleyite") or from W.-Y. Zhou et al. (2022) ("hydrous wadsleyite"). The elastic moduli for hydrous wadsleyite systematically result in stronger anisotropies than those estimated using elasticity data for dry wadsleyite. In addition, the geometry of the anisotropy can also be different (e.g., Vs anisotropy for models A and C).

The elastic moduli of W.-Y. Zhou et al. (2022) have been measured at lower P-T conditions than those of the MTZ and extrapolated. One may hence question whether the difference between "hydrous" and "dry" wadsleyite elasticity could be due to this extrapolation and not an effect of water content. We hence perform an additional test with the computed elastic moduli for hydrous wadsleyite of W. Wang et al. (2019) (Figure S5 in Supporting Information S1). The resulting seismic anisotropies are comparable to those found using the experimentally determined elastic moduli for hydrous wadsleyite from W.-Y. Zhou et al. (2022). Water content is likely to have a great impact on the wadsleyite elastic tensors at high P-T conditions based on the comparisons between Núñez-Valdez et al. (2013), W.-Y. Zhou et al. (2022), and W. Wang et al. (2019). It is noteworthy that the methods as well as wadsleyite's Fe contents in these three studies are different. More high P-T single-crystal elasticity studies will be needed to quantify the effect of water content on wadsleyite single-crystal elastic moduli at high P-T in the future.

5.2. Effect of Wadsleyite Texture Type on Anisotropy in the Transition Zone

In addition to the effect of water on the single crystal elastic moduli, Figure 5a also shows that the plasticity of wadsleyite will also depend on both temperature and water content, with implications on the resulting seismic anisotropy.

We hence test each wadsleyite plasticity model with both sets of dry and hydrous wadsleyite elastic properties. Figure 5b shows the results for anisotropy after simulations with deformation in shear up to $\gamma = 1$. They are summarized below:

- Type-A deformation combined with dry wadsleyite elasticity results in a moderate anisotropy, with a P-wave azimuthal anisotropy of 2.1% and a fast propagation direction at low angle to the shear direction, and a maximum S-waves splitting (ΔV_S) of 2.3% in the plane normal to the shear direction. The same deformation model using hydrous wadsleyite elasticity enhances seismic anisotropy, with a P-wave azimuthal anisotropy of 6.3%, and ΔV_S up to 5.3%.
- Type-B deformation combined with dry wadsleyite elasticity leads to weak anisotropy, with both P-wave azimuthal anisotropy and ΔV_S largely under 1%. Type-B deformation with hydrous wadsleyite elasticity, however, results in 3.4% P-wave azimuthal anisotropy, with a fast propagation direction normal to the shear

Figure 5. Deformation map of wadsleyite versus temperature and water content and corresponding predicted seismic signal. (a) Dominant wadsleyite texture type based on observations from this study (stars), Couvy (2005) (diamonds), Demouchy et al. (2011) (circles), Kawazoe et al. (2013) (triangles) and Ohuchi et al. (2014) (squares). The observed texture type is color-coded, red for Type-A, yellow for Type-B, blue for Type-C and orange for Type-E. Mixed yellow and blue markers are observations which could match both the Type-B or Type-C textures. For each texture type, the figure also provides the list of active slip systems, in decreasing order of relative activity. (b) Corresponding seismic anisotropy for texture Types-A, B, C, D, and E simulated after a shear deformation of $\gamma = 1$, and for both cases of dry and hydrous wadsleyite. In the case of dry wadsleyite, the elastic moduli of Núñez-Valdez et al. (2013) are used to compute the seismic anisotropy, while the elastic moduli of W.-Y. Zhou et al. (2022) are used in case of hydrous wadsleyite (see Table S1 in Supporting Information S1). The direction of shear is shown in the figure. Texture type D is not observed in experiments (see text). The computed elastic constants for the polycrystal are reported in Table S2 of Supporting Information S1.

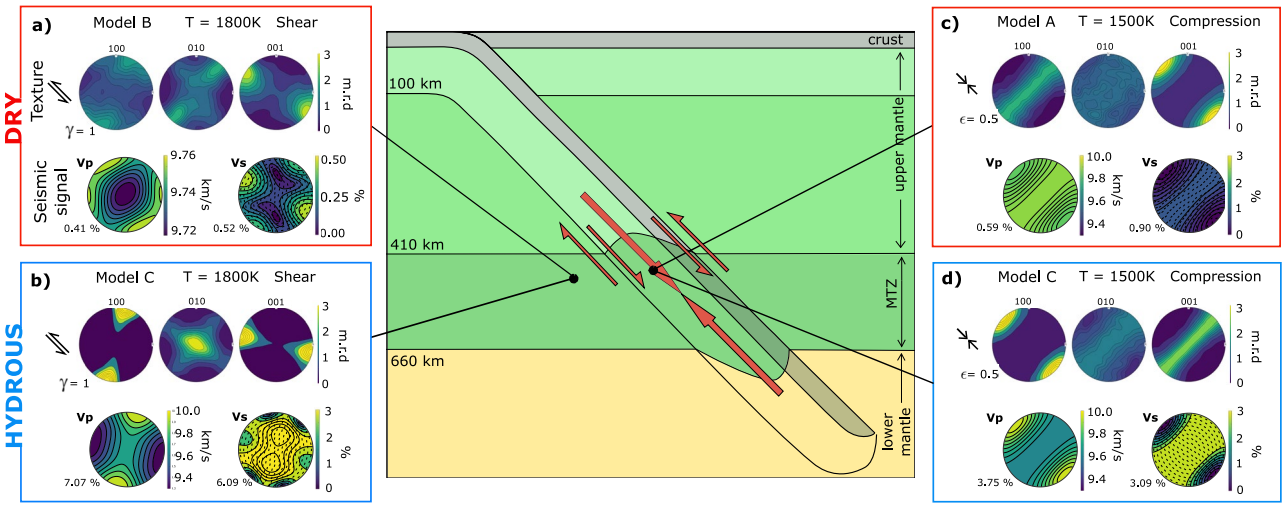

Figure 6. Modeled textures and anisotropy in wadsleyite in the upper part of the mantle transition zone near a subduction zone, assuming either a dry (a, c) or hydrous (b, d) mantle. The plastic models for wadsleyite are based on the deformation map of Figure 5. The elastic constants used for the seismic anisotropies computations are from the study of Núñez-Valdez et al. (2013) for dry wadsleyite (a, c) and from W.-Y. Zhou et al. (2022) for hydrous wadsleyite (b, d). Deformation inside the slab is assumed in compression, parallel to the subduction direction. Deformation below the slab is in shear, with the shear plane parallel to the slab. Deformation was modeled up to $\gamma = 1$ in shear and 50% in compression.

plane. ΔV_S with hydrous elasticity reaches 1.9% with a maximum of splitting in the shear plane, normal to the shear direction.

- Type-C deformation with dry wadsleyite elasticity shows a moderate P-wave azimuthal anisotropy of 2.4% with a fast direction close to the normal to the shear plane, and a ΔV_S of up to 2.5%, with a maximum in a plane close to the shear plane. Type-C deformation with hydrous wadsleyite elasticity leads to a strong P-wave azimuthal anisotropy of 7.1% with a fast direction normal to the shear plane, and ΔV_S of up to 6.1%, with two maxima normal to the shear direction, at low angle of the shear plane.
- Dry wadsleyite elasticity and type-D deformation gives rise to a strong anisotropy, with a P-wave azimuthal anisotropy of 4.3% with a fast direction close to the normal to the shear plane, and ΔV_S of up to 4.0%, with a maximum normal to the shear direction in the shear plane. Type-D deformation with hydrous elasticity leads to strong anisotropy (5.2% in V_P and up to 6.1% in ΔV_S), albeit with a complex geometry which may be hard to evaluate in a natural setting.
- Finally, Type-E deformation with dry wadsleyite elasticity is associated with a strong anisotropy (similarly to Type-D), characterized by a P-wave azimuthal anisotropy of 4.5% with a fast direction almost in the shear direction, and ΔV_S of up to 4.2%, with a maximum normal to the shear direction in the shear plane. As for Type-D deformation, Type-E deformation with hydrous elasticity leads to strong anisotropy with a complex geometry.

5.3. A Simple Model of Mantle Anisotropy in a Subduction Zone

As highlighted above, both temperature and water content strongly affect predictions of seismic anisotropy. In order to allow a simple comparison between the results of this work and seismic observations, we propose to model mantle seismic anisotropy in the context of simple models of deformation in the MTZ.

We assume a simple geological setting, with a slab subducting at 45° in the ambient mantle (Figure 6) and investigate two distinct regions of deformation: the ambient mantle close to the slab, in which we assume shear parallel to the slab face; and the mantle inside the subducting slab, with a compression deformation regime. We then compute the seismic anisotropy for wadsleyite in the MTZ for each of these settings, testing both hypotheses of a dry and hydrous MTZ.

In these models we assume elasticity at 1800 K and 15 GPa for the wadsleyite of the MTZ and at 1500 K and 15 GPa in the slab (Table S1 in Supporting Information S1). Both temperature and pressure only weakly affect anisotropy calculation results with MTZ conditions. Based on the results of Figure 5, the active slip systems and

elastic properties of wadsleyite (and so the corresponding anisotropy) depend on water content and temperature. We hence vary the deformation model and the elastic moduli depending on the geological setting and the level of hydration of the Earth's mantle.

In the ambient sheared mantle, near the faces of the slab, we expect temperatures close to those of the geotherm, 1700–1800 K (e.g., Katsura, 2022; Katsura et al., 2004). In such scenario, we expect dry wadsleyite to follow the Type-B deformation model, with a resulting V_P and V_S anisotropy of less than 0.5% (Figure 6a). Hydrous wadsleyite would follow the Type-C deformation model, leading to strong anisotropy, with V_P azimuthal anisotropy of 7.1% and a fast propagation direction close to the normal to the slab, and shear wave splitting of up to 6.1% with a maximum splitting parallel to the trench (Figure 6b).

Inside the subducted slab, where the temperatures are below 1700 K, we can expect plastic models A or C to be dominant in wadsleyite, depending on the water content. In the case of a completely dry wadsleyite in the slab, texture A will develop, with a weak anisotropy, below 1%, for both V_P and V_S (Figure 6c). If wadsleyite is hydrous, however, seismic anisotropy can be significant with 3.75% V_P azimuthal anisotropy and a fast propagation direction parallel to the slab dip, and shear wave splitting of up to 3.09%, with maximum splitting in the plane normal to the slab dip (Figure 6d).

5.4. Comparison With Observations

To our knowledge, no seismic study managed to isolate the seismic signal produced inside a subducting slab in the MTZ. Seismic anisotropy in subduction zones, however, has been extensively measured (e.g., Foley & Long, 2011; Huang et al., 2019; Lynner & Long, 2015; Mohiuddin et al., 2015; Montagner et al., 2021; Nowacki et al., 2015; H. Zhang et al., 2021) and seismic observations for the mantle around the slab have been reported.

Seismic signals measured in the MTZ near subduction zones depend on the region of study, with observations of S waves fast directions parallel to the trench (Foley & Long, 2011; Mohiuddin et al., 2015; Nowacki et al., 2015), parallel to the subduction direction (Nowacki et al., 2015), parallel to the slab geometry (Mohiuddin et al., 2015; Nowacki et al., 2015), normal to the trench (Huang et al., 2019), or even varying within the same subduction zone (Mohiuddin et al., 2015; Nowacki et al., 2015). In addition, different studies sometimes propose different observations for a same region, as for the Tonga subduction zone (see Foley & Long, 2011; Mohiuddin et al., 2015; Nowacki et al., 2015). It is hence difficult to compare our model predictions of Figure 6 to seismic observations, overall, which seem to depend on the local geophysical context.

Despite these limitations, we can argue that our model for a dry mantle (Figures 6a and 6c) agrees with seismic measurements of a weak seismic anisotropy in the MTZ as observed by Panning and Romanowicz (2006). Hydrous mantle models produce strong anisotropy in wadsleyite, with maxima in ΔV_S at 45° of the trench direction. Yuan and Beghein (2013) have reported a seismic anisotropy of 1% in the MTZ using higher mode surface waves. As these types of waves are less sensitive at depth deeper than the uppermost mantle, this measurement indicates a significant seismic anisotropy in the MTZ. Comparison with our models, however, is tricky, due to the different waves types used. Observations of weak seismic anisotropy in the MTZ, then, seem more consistent with our predictions in the case of a dry MTZ. Hence, based on these results, we might argue a rather dry MTZ, with less than 500 weight ppm H_2O.

As discussed in previous sections, however, the plasticity of wadsleyite is rather complex, with secondary slip systems that depend on external conditions and strongly affect the resulting microstructures and, hence, anisotropy. With this work, we offer predictions of anisotropy in wadsleyite in various geophysical settings, which will be available for interpreting seismic observations in further studies.

6. Conclusion

We deformed polycrystalline wadsleyite at pressures of 12.3–20.3 GPa and temperatures of 1450–1730 K in laser-heated diamond anvil cells on synchrotron beamlines and followed the orientations of individual grains in-situ using multigrain crystallography. Wadsleyite compression LPO under such conditions are characterized either (a) by [100] crystallographic axes oriented toward the compression direction, [010] axes close to the compression plane and the [001] axes normal to the compression direction, or (b) by [100] crystallographic axis at 30–40° of the compression direction, the [010] axis at 20–30° of the compression plane, and the [001] axis

normal to the compression direction. FOSO-VPSC modeling indicates that in the first case, the texture is well reproduced by dominant dislocation slip on the ⟨111⟩{101} slip system, with secondary contribution of [001](010) and no contribution of the [100]{0kl} system, as shown in our deformation model Type-C. The second texture observed in our samples is well reproduced in FOSO-VPSC by dominant slip on the ⟨111⟩{101} slip system, with secondary contributions of [001](010) and [100]{0kl}, labeled here as the Type-B plastic deformation model.

We then built a comprehensive summary of all published literature results on wadsleyite plastic deformation and propose an updated deformation map for wadsleyite. Clear trends can be noticed: (a) at low temperature and low water content, Type-A wadsleyite plasticity is dominant, associated with activation of the ⟨111⟩{101} and [100]{0kl} slip systems only; (b) at high temperature and low water content, Type-B wadsleyite plasticity is observed, associated with activation of the ⟨111⟩{101}, [100]{0kl} and [001](010) slip systems; *(c)* at high temperature and high water content, Type-C plasticity is observed, associated with activation of the ⟨111⟩{101} and [001](010) slip systems only. Observed experimental microstructures in polycrystalline wadsleyite are well modeled within dislocation creep. As inferred from numerical studies, ⟨111⟩{101} is the most active slip system in polycrystalline wadsleyite at all conditions. Secondary slip systems, however, depend on both temperature and water content and have a strong influence on the final microstructures.

In the Earth's mantle, wadsleyite plasticity will depend on the geological setting, and in particular on conditions of temperature and hydration of the MTZ. The resulting anisotropy depends on the plasticity model, but also the choice of single crystal elastic moduli, which have a significant influence on the final results. To first order, we find that our models with water-poor wadsleyite plasticity tend to provide the best match to the seismic observations of weak anisotropy in the MTZ. These conclusions, however, seem to vary regionally and should be updated as resolution improves in seismological studies.

In the future, these results would be improved by investigating the behavior of wadsleyite at low temperatures and high water content, and constraining the detailed conditions of transitions between the dominant plasticity models. The effect of strain rate, as well, remains ill-understood. Numerical models indicate that, under mantle strain rates, pure climb and diffusion creep should dominate plastic deformation in most of the MTZ, apart from regions with larger stresses, such as cold subducting slabs, in which dislocation glide could dominate (Ritterbex et al., 2020). In the lower mantle for example, extremely low strain-rates as encountered in situ might significantly affect the assemblage rheology (Cordier et al., 2023). Further experimental confirmation of this process would be welcome. Finally, our results show that anisotropy models of the Earth's MTZ strongly depend on the choice of published sets of single crystal elastic moduli. As such, the study of the elastic properties of wadsleyite as well as the combined effects of water, chemical composition, pressure, and temperature, remain a fundamental question for understanding the processes in the Earth's mantle on the basis of seismic observations.

Conflict of Interest

The authors declare no conflicts of interest relevant to this study.

Data Availability Statement

Datasets for this research include our data from the MGC diffraction images and files necessary for their treatment, for each measurement presented. We also provide the input files used for our FOSO-VPSC simulations, as well as the Cij for the polycrystal computed from these simulations. All are provided in Ledoux, Saki, et al. (2023).

Acknowledgments
We acknowledge the European Synchrotron Radiation Facility for provision of synchrotron radiation facilities on the ID27 beamline. We acknowledge DESY (Hamburg, Germany), a member of the Helmholtz Association HGF, for the provision of experimental facilities. Parts of this research were carried out at PETRA III using the P02.2 beamline. Beamtime was allocated for proposal ID20170278EC. The authors acknowledge the Chevreul Institute and the Lille electron microscopy platform in the development of this work through the ARCHI-CM project supported by the "Ministère de l'Enseignement Supérieur de la Recherche et de l'Innovation," the région "Hauts-de-France," the ERDF program of the European Union and the "Métropole Européenne de Lille." The authors also thank Marine Colleit for help on the first experiments, Jannick Ingrin for the FTIR analysis of our starting material, Ahmed Addad for assistance with the SEM measurements, and Jonathan Wright for assistance in data processing. The study was financed by the bilateral ANR-DFG TIMEleSS project (ANR-17-CE31-0025; TH 1530/18-1; SA 2585/3-1; SP1216/8-1; BY101/2-1) and the bilateral PROCOPE-PPP program (Campus France PHC 40555PC; DAAD 57390184). The research leading to this result has been supported by the project CALIPSOplus under the Grant Agreement 730872 from the EU Framework Programme for Research and Innovation HORIZON 2020.

References

Andrault, D., & Bolfan-Casanova, N. (2022). Mantle rain toward the Earth's surface: A model for the internal cycle of water. *Physics of the Earth and Planetary Interiors*, *322*, 106815. https://doi.org/10.1016/j.pepi.2021.106815

Angel, R. J., Alvaro, M., & Gonzalez-Platas, J. (2014). EosFit7c and a Fortran module (library) for equation of state calculations. *Zeitschrift für Kristallographie - Crystalline Materials*, *229*(5), 405–419. https://doi.org/10.1515/zkri-2013-1711

Angel, R. J., Alvaro, M., & Nestola, F. (2018). 40 years of mineral elasticity: A critical review and a new parameterisation of equations of state for mantle olivines and diamond inclusions. *Physics and Chemistry of Minerals*, *45*(2), 95–113. https://doi.org/10.1007/s00269-017-0900-7

Bachmann, F., Hielscher, R., & Schaeben, H. (2010). Texture analysis with MTEX – Free and open source software toolbox. *Solid State Phenomena*, *160*, 63–68. https://doi.org/10.4028/www.scientific.net/SSP.160.63

Bercovici, D., & Karato, S.-I. (2003). Whole-mantle convection and the transition-zone water filter. *Nature*, *425*(6953), 39–44. https://doi.org/10.1038/nature01918

Buchen, J., Marquardt, H., Speziale, S., Kawazoe, T., Ballaran, T. B., & Kurnosov, A. (2018). High-pressure single-crystal elasticity of wadsleyite and the seismic signature of water in the shallow transition zone. *Earth and Planetary Science Letters*, *498*, 77–87. https://doi.org/10.1016/j.epsl.2018.06.027

Castaneda, P. P., & Suquet, P. (1997). Nonlinear composites. *Advances in Applied Mechanics*, *34*, 171–302. https://doi.org/10.1016/s0065-2156(08)70321-1

Castelnau, O., Derrien, K., Ritterbex, S., Carrez, P., Cordier, P., & Moulinec, H. (2021). Multiscale modeling of the effective viscoplastic behavior of Mg_2Si0_4 wadsleyite: Bridging atomic and polycrystal scales. *Comptes Rendus Mecanique*, *348*(10–11), 827–846. https://doi.org/10.5802/crmeca.61

Chandler, B., Bernier, J., Diamond, M., Kunz, M., & Wenk, H.-R. (2021). Exploring microstructures in lower mantle mineral assemblages with synchrotron X-rays. *Science Advances*, *7*(1), eabd3614. https://doi.org/10.1126/sciadv.abd3614

Chandler, B., Devoe, M., Kunz, M., & Wenk, H.-R. (2021). Using multigrain crystallography to explore the microstructural evolution of the α-olivine to γ-ringwoodite transformation and ϵ-Mg_2SiO_4 at high pressure and temperature. *Minerals*, *11*(4), 424. https://doi.org/10.3390/min11040424

Cordier, P., Gouriet, K., Weidner, T., Van Orman, J., Castelnau, O., Jackson, J. M., & Carrez, P. (2023). Periclase deforms more slowly than bridgmanite under mantle conditions. *Nature*, *613*(7943), 303–307. https://doi.org/10.1038/s41586-022-05410-9

Couvy, H. (2005). Experimental deformation of forsterite, wadsleyite and ringwoodite: Implications for seismic anisotropy of the Earth's mantle (Unpublished doctoral dissertation).

Demouchy, S., Mainprice, D., Tommasi, A., Couvy, H., Barou, F., Frost, D., & Cordier, P. (2011). Forsterite to wadsleyite phase transformation under shear stress and consequences for the Earth's mantle transition zone. *Physics of the Earth and Planetary Interiors*, *184*(1), 91–104. https://doi.org/10.1016/j.pepi.2010.11.001

Faccenda, M. (2014). Mid mantle seismic anisotropy around subduction zones. *Physics of the Earth and Planetary Interiors*, *227*, 1–19. https://doi.org/10.1016/j.pepi.2013.11.015

Farla, R., Amulele, G., Girard, J., Miyajima, N., & Karato, S.-i. (2015). High-pressure and high-temperature deformation experiments on polycrystalline wadsleyite using the rotational Drickamer apparatus. *Physics and Chemistry of Minerals*, *42*(7), 541–558. https://doi.org/10.1007/s00269-015-0742-0

Foley, B. J., & Long, M. D. (2011). Upper and mid-mantle anisotropy beneath the Tonga slab. *Geophysical Research Letters*, *38*(2), L02303. https://doi.org/10.1029/2010GL046021

Fukao, Y., Widiyantoro, S., & Obayashi, M. (2001). Stagnant slabs in the upper and lower mantle transition region. *Reviews of Geophysics*, *39*(3), 291–323. https://doi.org/10.1029/1999RG000068

Gay, J. P., Ledoux, E., Krug, M., Chantel, J., Pakhomova, A., Liermann, H.-P., et al. (2023). Transformation microstructures in pyrolite under stress: Implications for anisotropy in subducting slabs below the 660 km discontinuity. *Earth and Planetary Science Letters*, *604*, 118015. https://doi.org/10.1016/j.epsl.2023.118015

Huang, Q., Schmerr, N., Waszek, L., & Beghein, C. (2019). Constraints on seismic anisotropy in the mantle transition zone from long-period SS precursors. *Journal of Geophysical Research: Solid Earth*, *124*(7), 6779–6800. https://doi.org/10.1029/2019JB017307

Karato, S.-I. (1998). Seismic anisotropy in the deep mantle, boundary layers and the geometry of mantle convection. *Pure and Applied Geophysics*, *151*(2–4), 23–587. https://doi.org/10.1007/s000240050130

Karato, S.-I., Jung, H., Katayama, I., & Skemer, P. (2008). Geodynamic significance of seismic anisotropy of the upper mantle: New insights from laboratory studies. *Annual Review of Earth and Planetary Sciences*, *36*(1), 59–95. https://doi.org/10.1146/annurev.earth.36.031207.124120

Katsura, T. (2022). A revised adiabatic temperature profile for the mantle. *Journal of Geophysical Research: Solid Earth*, *127*(2), e2021JB023562. https://doi.org/10.1029/2021jb023562

Katsura, T., Shatskiy, A., Manthilake, M. A. G. M., Zhai, S., Yamazaki, D., Matsuzaki, T., et al. (2009). *P-V-T* relations of wadsleyite determined by in situ X-ray diffraction in a large-volume high-pressure apparatus. *Geophysical Research Letters*, *36*(11), L11307. https://doi.org/10.1029/2009GL038107

Katsura, T., Yamada, H., Nishikawa, O., Song, M., Kubo, A., Shinmei, T., et al. (2004). Olivine-wadsleyite transition in the system $(Mg,Fe)_2SiO_4$. *Journal of Geophysical Research*, *109*(B2), B02209. https://doi.org/10.1029/2003JB002438

Kawazoe, T., Ohuchi, T., Nishihara, Y., Nishiyama, N., Fujino, K., & Irifune, T. (2013). Seismic anisotropy in the mantle transition zone induced by shear deformation of wadsleyite. *Physics of the Earth and Planetary Interiors*, *216*, 91–98. https://doi.org/10.1016/j.pepi.2012.12.005

Kiefer, B., Stixrude, L., Hafner, J., & Kresse, G. (2001). Structure and elasticity of wadsleyite at high pressures. *American Mineralogist*, *86*(11–12), 1387–1395. https://doi.org/10.2138/am-2001-11-1207

Kimura, T., Ohfuji, H., Nishi, M., & Irifune, T. (2017). Melting temperatures of MgO under high pressure by micro-texture analysis. *Nature Communications*, *8*(1), 15735. https://doi.org/10.1038/ncomms15735

Krug, M., Saki, M., Ledoux, E., Gay, J. P., Chantel, J., Pakhomova, A., et al. (2022). Textures induced by the coesite-stishovite transition and implications for the visibility of the X-discontinuity. *Geochemistry, Geophysics, Geosystems*, *23*(10), e2022GC010544. https://doi.org/10.1029/2022gc010544

Kupenko, I., Dubrovinsky, L., Dubrovinskaia, N., McCammon, C., Glazyrin, K., Bykova, E., et al. (2012). Portable double-sided laser-heating system for Mössbauer spectroscopy and X-ray diffraction experiments at synchrotron facilities with diamond anvil cells. *Review of Scientific Instruments*, *83*(12), 124501. https://doi.org/10.1063/1.4772458

Langrand, C., Hilairet, N., Nisr, C., Roskosz, M., Ribárik, G., Vaughan, G. B. M., & Merkel, S. (2017). Reliability of multigrain indexing for orthorhombic polycrystals above 1 Mbar: Application to $MgSiO_3$ post-perovskite. *Journal of Applied Crystallography*, *50*(1), 120–130. https://doi.org/10.1107/S1600576716018057

Lebensohn, R. A., Castañeda, P. P., Brenner, R., & Castelnau, O. (2011). Full-field vs. homogenization methods to predict microstructure–property relations for polycrystalline materials. *Computational methods for microstructure-property relationships*, 393–441. https://doi.org/10.1007/978-1-4419-0643-4_11

Lebensohn, R. A., & Tomé, C. (1993). A self-consistent anisotropic approach for the simulation of plastic deformation and texture development of polycrystals: Application to zirconium alloys. *Acta Metallurgica et Materialia*, *41*(9), 2611–2624. https://doi.org/10.1016/0956-7151(93)90130-K

Ledoux, E., Krug, M., Gay, J., Chantel, J., Hilairet, N., Bykov, M., et al. (2023). In-situ study of microstructures induced by the olivine to wadsleyite transformation at conditions of the 410 km depth discontinuity. *American Mineralogist*. https://doi.org/10.2138/am-2022-8731

Ledoux, E., Saki, M., Gay, J. P., Krug, M., Castelnau, O., Zhou, W.-Y., et al. (2023). Data supporting "Deformation mechanisms, microstructures, and seismic anisotropy of wadsleyite in the Earth's transition zone" by Ledoux et al. [Dataset]. Recherche Data Gouv. https://doi.org/10.57745/OVCWQN

Liermann, H.-P., Konôpková, Z., Morgenroth, W., Glazyrin, K., Bednarčík, J., McBride, E. E., et al. (2015). The extreme conditions beamline P02.2 and the extreme conditions science infrastructure at PETRA III. *Journal of Synchrotron Radiation*, *22*(4), 908–924. https://doi.org/10.1107/S1600577515005937

Lutterotti, L., Vasin, R., & Wenk, H.-R. (2014). Rietveld texture analysis from synchrotron diffraction images. I. Calibration and basic analysis. *Powder Diffraction*, *29*(1), 76–84. https://doi.org/10.1017/S0885715613001346

Lynner, C., & Long, M. D. (2015). Heterogeneous seismic anisotropy in the transition zone and uppermost lower mantle: Evidence from South America, Izu-Bonin and Japan. *Geophysical Journal International*, *201*(3), 1545–1552. https://doi.org/10.1093/gji/ggv099

Magali, J. K., Bodin, T., Hedjazian, N., Ricard, Y., Capdeville, Y., & Debayle, E. (2021). Quantifying intrinsic and extrinsic contributions to radial anisotropy in tomographic models. *Geophysical Journal International*, *126*(10), 1545–1552. https://doi.org/10.1029/2021jb022322

Mainprice, D., Barruol, G., & Ismaïl, B. (2000). The seismic anisotropy of the Earth's mantle: From single crystal to polycrystal. In S. Karato, A. M. Forte, R. C. Liebermann, G. Master, & L. Stixrude (Eds.), *Earth's deep interior: Mineral physics and tomography. from the atomic to the global scale* (Vol. 117, pp. 237–264). American Geophysical Union. https://doi.org/10.1029/GM117p0237

Mao, Z., Jacobsen, S. D., Frost, D. J., McCammon, C. A., Hauri, E. H., & Duffy, T. S. (2011). Effect of hydration on the single-crystal elasticity of Fe-bearing wadsleyite to 12 GPa. *American Mineralogist*, *96*(10), 1606–1612. https://doi.org/10.2138/am.2011.3807

Mao, Z., Jacobsen, S. D., Jiang, F., Smyth, J., Holl, C., & Duffy, T. (2008). Elasticity of hydrous wadsleyite to 12 GPa: Implications for Earth's transition zone. *Geophysical Research Letters*, *35*(21), L21305. https://doi.org/10.1029/2008GL035618

Metsue, A., Carrez, P., Denoual, C., Mainprice, D., & Cordier, P. (2010). Plastic deformation of wadsleyite: IV dislocation core modelling based on the Peierls-Nabarro-Galerkin model. *Acta Materialia*, *58*(5), 1467–1478. https://doi.org/10.1016/j.actamat.2009.10.047

Mezouar, M., Crichton, W., Bauchau, S., Thurel, F., Witsch, H., Torrecillas, F., et al. (2005). Development of a new state-of-the-art beamline optimized for monochromatic single-crystal and powder X-ray diffraction under extreme conditions at the ESRF. *Journal of Synchrotron Radiation*, *12*(5), 659–664. https://doi.org/10.1107/S0909049505023216

Miyajima, N., & Kawazoe, T. (2015). Dislocation microstructures in simple-shear-deformed wadsleyite at transition-zone conditions: Weak-beam dark-field tem characterization of dislocations on the (010) plane. *American Mineralogist*, *100*(11–12), 2749–2752. https://doi.org/10.2138/am-2015-5481

Mohiuddin, A., Long, M. D., & Lynner, C. (2015). Mid-mantle seismic anisotropy beneath southwestern Pacific subduction systems and implications for mid-mantle deformation. *Physics of the Earth and Planetary Interiors*, *245*, 1–14. https://doi.org/10.1016/j.pepi.2015.05.003

Montagner, J.-P., Burgos, G., Capdeville, Y., Beucler, E., & Mocquet, A. (2021). The mantle transition zone dynamics as revealed through seismic anisotropy. *Tectonophysics*, *821*, 229133. https://doi.org/10.1016/j.tecto.2021.229133

Nowacki, A., Kendall, J.-M., Wookey, J., & Pemberton, A. (2015). Mid-mantle anisotropy in subduction zones and deep water transport. *Geochemistry, Geophysics, Geosystems*, *16*(3), 764–784. https://doi.org/10.1002/2014GC005667

Núñez-Valdez, M., Da Silveira, P., & Wentzcovitch, R. M. (2011). Influence of iron on the elastic properties of wadsleyite and ringwoodite. *Journal of Geophysical Research*, *116*(B12), B12207. https://doi.org/10.1029/2011JB008378

Núñez-Valdez, M., Wu, Z., Yu, Y. G., & Wentzcovitch, R. M. (2013). Thermal elasticity of $(Fe_x, Mg_{1-x})_2SiO_4$ olivine and wadsleyite. *Geophysical Research Letters*, *40*(2), 290–294. https://doi.org/10.1002/grl.50131

Ohuchi, T., Fujino, K., Kawazoe, T., & Irifune, T. (2014). Crystallographic preferred orientation of wadsleyite and ringwoodite: Effects of phase transformation and water on seismic anisotropy in the mantle transition zone. *Earth and Planetary Science Letters*, *397*, 133–144. https://doi.org/10.1016/j.epsl.2014.03.066

Panning, M., & Romanowicz, B. (2006). A three-dimensional radially anisotropic model of shear velocity in the whole mantle. *Geophysical Journal International*, *167*(1), 361–379. https://doi.org/10.1111/j.1365-246X.2006.03100.x

Ponte Castañeda, P. (2015). Fully optimized second-order variational estimates for the macroscopic response and field statistics in viscoplastic crystalline composites. *Proceedings of the Royal Society A: Mathematical, Physical and Engineering Sciences*, *471*(2184), 20150665. https://doi.org/10.1098/rspa.2015.0665

Prescher, C., & Prakapenka, V. B. (2015). *DIOPTAS*: A program for reduction of two-dimensional x-ray diffraction data and data exploration. *High Pressure Research*, *35*(3), 223–230. https://doi.org/10.1080/08957959.2015.1059835

Ringwood, A. (1991). Phase transformations and their bearing on the constitution and dynamics of the mantle. *Geochimica et Cosmochimica Acta*, *55*(8), 2083–2110. https://doi.org/10.1016/0016-7037(91)90090-R

Ritterbex, S., Carrez, P., & Cordier, P. (2020). Deformation across the mantle transition zone: A theoretical mineral physics view. *Earth and Planetary Science Letters*, *547*, 116438. https://doi.org/10.1016/j.epsl.2020.116438

Ritterbex, S., Carrez, P., & Cordier, P. (2016). Modeling dislocation glide and lattice friction in Mg_2SiO_4 wadsleyite in conditions of the Earth's transition zone. *American Mineralogist*, *101*(9), 2085–2094. https://doi.org/10.2138/am-2016-5578CCBYNCND

Rosa, A. D., Hilairet, N., Ghosh, S., Garbarino, G., Jacobs, J., Perrillat, J.-P., et al. (2015). *In situ* monitoring of phase transformation microstructures at Earth's mantle pressure and temperature using multi-grain XRD. *Journal of Applied Crystallography*, *48*(5), 1346–1354. https://doi.org/10.1107/S1600576715012765

Rosa, A. D., Hilairet, N., Ghosh, S., Perrillat, J.-P., Garbarino, G., & Merkel, S. (2016). Evolution of grain sizes and orientations during phase transitions in hydrous Mg_2SiO_4. *Journal of Geophysical Research: Solid Earth*, *121*(10), 7161–7176. https://doi.org/10.1002/2016JB013360

Sharp, T. G., Bussod, G. Y. A., & Katsura, T. (1994). Microstructures in β-$Mg_{1.8}Fe_{0.2}SiO_4$ experimentally deformed at transition-zone conditions. *Physics of the Earth and Planetary Interiors*, *86*(1–3), 69–83. https://doi.org/10.1016/0031-9201(94)05062-7

Shen, G., & Lazor, P. (1995). Measurement of melting temperatures of some minerals under lower mantle pressures. *Journal of Geophysical Research*, *100*(B9), 17699–17713. https://doi.org/10.1029/95jb01864

Sinogeikin, S., Katsura, T., & Bass, J. (1998). Sound velocities and elastic properties of Fe-bearing wadsleyite and ringwoodite. *Journal of Geophysical Research*, *103*(B9), 20819–20825. https://doi.org/10.1029/98JB01819

Smyth, J. R., Miyajima, N., Huss, G. R., Hellebrand, E., Rubie, D. C., & Frost, D. J. (2012). Olivine-wadsleyite-pyroxene topotaxy: Evidence for coherent nucleation and diffusion-controlled growth at the 410-km discontinuity. *Physics of the Earth and Planetary Interiors*, *200–201*, 85–91. https://doi.org/10.1016/j.pepi.2012.04.003

Song, D., & Ponte Castañeda, P. (2018). Fully optimized second-order homogenization estimates for the macroscopic response and texture evolution of low-symmetry viscoplastic polycrystals. *International Journal of Plasticity*, *110*, 272–293. https://doi.org/10.1016/j.ijplas.2018.07.004

Thurel, E., & Cordier, P. (2003). Plastic deformation of wadsleyite: I. High-pressure deformation in compression. *Physics and Chemistry of Minerals*, *30*(5), 256–266. https://doi.org/10.1007/s00269-003-0312-8

Thurel, E., Douin, J., & Cordier, P. (2003). Plastic deformation of wadsleyite: III. Interpretation of dislocations and slip systems. *Physics and Chemistry of Minerals*, *30*(5), 271–279. https://doi.org/10.1007/s00269-003-0314-6

Tommasi, A., Mainprice, D., Cordier, P., Thoraval, C., & Couvy, H. (2004). Strain-induced seismic anisotropy of wadsleyite polycrystals and flow patterns in the mantle transition zone. *Journal of Geophysical Research*, *109*(B12), B12405. https://doi.org/10.1029/2004JB003158

Van Der Hilst, R. D., Widiyantoro, S., & Engdahl, E. R. (1997). Evidence for deep mantle circulation from global tomography. *Nature*, *386*(6625), 578–584. https://doi.org/10.1038/386578a0

Wang, J., Bass, J. D., & Kastura, T. (2014). Elastic properties of iron-bearing wadsleyite to 17.7 GPa: Implications for mantle mineral models. *Physics of the Earth and Planetary Interiors*, *228*, 92–96. https://doi.org/10.1016/j.pepi.2014.01.015

Wang, W., Walter, M. J., Peng, Y., Redfern, S., & Wu, Z. (2019). Constraining olivine abundance and water content of the mantle at the 410-km discontinuity from the elasticity of olivine and wadsleyite. *Earth and Planetary Science Letters*, *519*, 1–11. https://doi.org/10.1016/j.epsl.2019.04.018

Wenk, H.-R., Lutterotti, L., Kaercher, P., Kanitpanyacharoen, W., Miyagi, L., & Vasin, R. (2014). Rietveld texture analysis from synchrotron diffraction images. II. Complex multiphase materials and diamond anvil cell experiments. *Powder Diffraction*, *29*(3), 220–232. https://doi.org/10.1017/S0885715614000360

Yuan, K., & Beghein, C. (2013). Seismic anisotropy changes across upper mantle phase transitions. *Earth and Planetary Science Letters*, *374*, 132–144. https://doi.org/10.1016/j.epsl.2013.05.031

Zhang, H., Schmandt, B., & Zhang, J. S. (2021). Localized anisotropy in the mantle transition zone due to flow through slab gaps. *Geophysical Research Letters*, *48*(10), e2021GL092712. https://doi.org/10.1029/2021GL092712

Zhang, J. S., Bass, J. D., & Schmandt, B. (2018). The elastic anisotropy change near the 410-km discontinuity: Predictions from single-crystal elasticity measurements of olivine and wadsleyite. *Journal of Geophysical Research: Solid Earth*, *123*(4), 2674–2684. https://doi.org/10.1002/2017JB015339

Zhou, D., Dong, J., Si, Y., Zhu, F., & Li, J. (2020). Melting curve of potassium chloride from in situ ionic conduction measurements. *Minerals*, *10*(3), 250. https://doi.org/10.3390/min10030250

Zhou, W.-Y., Hao, M., Zhang, J. S., Chen, B., Wang, R., & Schmandt, B. (2022). Constraining composition and temperature variations in the mantle transition zone. *Nature Communications*, *13*(1), 1094. https://doi.org/10.1038/s41467-022-28709-7

Zhou, W.-Y., Ren, Z., Zhang, J. S., Chen, B., Hao, M., Ohuchi, T., et al. (2021). The water-Fe-pressure dependent single-crystal elastic properties of wadsleyite: Implications for the seismic anisotropy in the upper mantle transition zone. *Earth and Planetary Science Letters*, *565*, 116955. https://doi.org/10.1016/j.epsl.2021.116955